Modeling of Magnetized Graphene from Microwave to THz Range by DGTD with a Scalar RBC and an ADE

Ping Li, *Member, IEEE,* and Li Jun Jiang, *Senior Member, IEEE*

Abstract—This paper presents a discontinuous Galerkin time domain (DGTD) method for the transient analysis of magnetized graphene from the microwave to terahertz (THz) frequencies. By considering the atom thick graphene layer as an infinitely thin conductive sheet with finite surface conductivity, a frequency dependent anisotropic resistive boundary condition (RBC) is obtained. Based on this RBC, the direct volumetric discretization of graphene layer is avoided. Instead of directly deriving the numerical flux for DGTD considering the presence this anisotropic and dispersive RBC, an auxiliary surface polarization current governed by a first-order time-dependent partial differential equation (PDE) is introduced over the graphene with the purpose to obtain an isotropic and simultaneously non-dispersive RBC. In this way, the new formulated numerical flux expression derived from the *Rankine-Hugoniot jump relations* is isotropic, and no time-domain convolution is involved in the finalized matrix equations. To verify the applicability and accuracy of the proposed algorithm, the Faraday rotation and the surface plasmon resonance of a plane wave through magnetically biased graphene are investigated. For open-region scattering problems, a hybrid DGTD and time-domain boundary integral (TDBI) method is applied to rigorously truncate the computational domain.

Index Terms—Auxiliary differential equation (ADE), anisotropic resistive boundary condition (RBC), discontinuous Galerkin time-domain (DGTD) method, magnetized graphene, time-domain boundary integral (TDBI) algorithm.

I. INTRODUCTION

AS a truly two-dimensional (2-D) layer with carbon atoms arranged in a honeycomb lattice, graphene has received significant attentions due to its many unusual physical properties [1] such as gapless electronic band structure, linear energy-momentum dispersion relationship, ambipolarity, and anomalous quantum Hall effect, etc. These remarkable features make it as a promising candidate for transistors [2], tuneable terahertz (THz) antennas [3], and surface plasmon waveguides [4], etc. The atom-thick graphene is best described by a surface conductivity which manipulates the electromagnetic/optical properties of graphene. In the absence of external magnetostatic biasing, the surface conductivity σ_g is a scalar [5], otherwise it becomes a tensor $\overline{\overline{\sigma}}_g$ [5], [9]. By dynamically tuning the surface conductivity via electrical or chemical doping, the propagation, polarization, radiation, and scattering of electromagnetic waves through graphene can be flexibly manipulated. The magnetically biased graphene

P. Li and L. J. Jiang are with the Department of Electrical and Electronic Engineering, The University of Hong Kong, Hong Kong, China (liping@eee.hku.hk, jianglj@hku.hk).

exhibits strong gyrotropic properties [6], [7] making it a promising candidate for microwave and optical components such as circulators, isolators, phase shifters and other non-reciprocal devices [7], [8]. Apart from the practical experimental demonstration of the gyrotropic properties like Faraday rotation, full-wave simulators are also necessary to implement numerical investigation.

For the situation without the magnetostatic biasing, a number of numerical solvers have already been developed to quantify the intrinsic properties of graphene such as method of moments (MoM) [10], finite-difference time-domain (FDTD) method [11]. Compared with frequency domain methods [10], time-domain methods [11], [12] have a plethora of advantages such as broadband characterization with only one single simulation, etc. To model the graphene, presently, there are two general approaches: i) The graphene is considered as a thin layer with finite thickness [14], [15], thus volumetric discretization is required. For this approach, the isotropic surface conductivity is transformed to an equivalent volume permittivity. ii) The graphene is modeled as an infinitesimal thin conductive sheet over which a scalar resistive boundary condition (RBC) is satisfied [11]–[13]. For the first approach, particularly fine spatial mesh structures are unavoidable, which is prohibitive for both memory cost and time consuming. On the other hand, the second approach by employing the RBC is free of these drawbacks.

In the presence of a biasing magnetic field, an anisotropic surface conductivity $\overline{\overline{\sigma}}_g$ [5], [6], [9] is generated due to Lorentz force, which significantly complicates the problem, thus novel methods must be developed to attack both the anisotropy and the dispersion. In [16], a matrix exponential FDTD method based on the direct volumetrically meshing is developed to analyze a free-standing magnetized graphene sheet illuminated by a plane wave. Via direct 3D discretization, the $\overline{\overline{\sigma}}_g$ is transformed to an equivalent volumetric tensor permittivity $\overline{\overline{\epsilon}}_g$. By introducing an auxiliary polarization volume current source governed by an auxiliary differential equation (ADE) into the Ampere's law equation, the anisotropic constitutive relation becomes isotropic (or scalar) and nondispersive. Therefore, the standard FDTD can be applied to the finalized partial differential equations (PDEs). Notably, straightforward volumetric discretization is the bottleneck of this method. Hence, the RBC based approaches are desired alternatives.

In this paper, a discontinuous Galerkin time-domain (DGTD) [18]–[20] method is developed for the first time to analyze the intrinsic properties of magnetically biased graphene by

leveraging the advantages of RBC. Compared with FDTD, DGTD is capable of modeling complex structures and easily achieve high order accuracy by using high-order basis functions. Unlike FEM [21], all operations of DGTD are local since the information exchange among neighboring elements are enforced through the numerical flux, thus resulting in block-diagonal mass and stiffness matrices. The dimension of each block is equal to the degrees of freedom (DoF) in that element. Mass-matrix blocks are inverted and stored before time marching, which produces a very compact and efficient solver when combined with an explicit scheme.

In DGTD analysis, all boundary conditions are implemented through reformulating the numerical flux based on the *Rankine-Hugoniot jump relations*. For a magnetized graphene, the anisotropic surface conductivity $\overline{\overline{\sigma}}_g$ will definitely result in an anisotropic RBC. Direct incorporation of this anisotropic R-BC into DGTD will no doubt result a numerical flux in a tensor scheme, simultaneously dispersive. To attack these problems, in this paper, an auxiliary surface polarization current governed by an ADE [16], [19], [23] is introduced over the graphene sheet. With the ADE and the auxiliary polarization current, the anisotropic and dispersive RBC is converted to be an isotropic and nondispersive one. Therefore, the time-domain convolution is avoided and the corresponding numerical flux in the presence of the new RBC is isotropic. With this approach, in fact, the gyroelectric effects are represented by the auxiliary polarization current, and the dispersive property is considered in the time-dependent ADE. By applying the DG testing over the two first-order Maxwell's curl equations and the ADE, the finalized semi-discrete matrix equations will be solved by the explicit Runge-Kutta (RK) marching scheme in this work. For PDE solvers, artificial boundaries must be enforced to truncate the computational region. In this work, DGTD is hybridized with the time-domain boundary integral (TDBI) algorithm by evaluating the field values required for the incoming numerical flux calculation over the truncation boundary [26]. This method is mathematically exact, and the truncation boundary can be conformal to the scatterer's surface, thus making the computational region as small as possible.

The remainder of this paper is organized as follows. In Section II, the theory and formulation of the proposed algorithm are detailed, including the description of RBC, the derivation of numerical flux and ADE, and the formulation of semi-discrete matrix equations. In Section III, numerical results are presented to validate the accuracy and robustness of the proposed algorithm. Conclusions are made at the end of this paper.

II. THEORY AND FORMULATION

A. Formulation of Upwind Flux with an Auxiliary Differential Equation

Suppose a graphene sheet is placed at $z = 0$ plane and biased by a static magnetic field perpendicular to the graphene plane, i.e., $\mathbf{B}_0 = \hat{\mathbf{z}} B_0$. Because of the Lorentz force, the surface conductivity exhibits anisotropy [7]. To have a fundamental insight into this phenomenon, the motion of an electron in the presence of an electric field $\mathbf{E}$ is studied. Firstly, a x-ploarized electric field $\mathbf{E} = \hat{\mathbf{x}} E_x$ is considered. In this case,

the electron is accelerated along the negative x-direction due to the electric force $\mathbf{F}_e = -e\mathbf{E}$ with $-e$ denoting the electron charge. Simultaneously, the moving electron with velocity $\boldsymbol{v}$ will expose to a Lorentz force $\mathbf{F}_m = -e\boldsymbol{v} \times \mathbf{B}_0$ along the negative $y-$ direction. As a result, two current components along the $x-$ and $y-$ directions respectively will be generated due to the entanglement of these two forces [7]. Namely,

$$\mathbf{J} = \sigma_{xx} E_x \hat{\mathbf{x}} + \sigma_{yx} E_x \hat{\mathbf{y}} \tag{1}$$

where σ_{xx} and σ_{yx} are conductivities parallel and perpendicular to the electric field $\mathbf{E}$, respectively. Similarly, for the case with an electric field $\mathbf{E} = \hat{\mathbf{y}} E_y$, two current components will be generated as well. That is,

$$\mathbf{J} = -\sigma_{xy} E_y \hat{\mathbf{x}} + \sigma_{yy} E_y \hat{\mathbf{y}} \tag{2}$$

For graphene with same properties in all directions, the conductivities must satisfy $\sigma_{xx} = \sigma_{yy}$ and $\sigma_{yx} = \sigma_{xy}$. Based on this fact, the generated currents in (1) and (2) can be combined together and rewritten into a compact form [7],

$$\mathbf{J} = \overline{\overline{\sigma}}_g \cdot \mathbf{E} \tag{3}$$

with $\mathbf{E} = [E_x, E_y, 0]^T$ and

$$\overline{\overline{\sigma}}_g = \begin{bmatrix} \sigma_{xx} & -\sigma_{yx} & 0 \\ \sigma_{yx} & \sigma_{xx} & 0 \\ 0 & 0 & 0 \end{bmatrix} \tag{4}$$

The analytical expressions for the surface conductivities σ_{xx} and σ_{yx} comprising intraband and interband contributions can be obtained based on the Kubo formula [22]. For frequencies in the THz range, the intraband term is dominant over the interband [7]. Thus, only the contribution from the intraband is considered in this paper. Based on the fact that the probability of electron transitions between Landau levels around the Fermi-level μ_c are the strongest over others, the expressions for σ_{xx} and σ_{yx} can be approximated by a Drude-like model [7], [16]. Namely,

$$\sigma_{xx}(\omega, \mu_c, \tau, T, B_0) = \sigma_0 \frac{1 + j\omega\tau}{(\omega_c \tau)^2 + (1 + j\omega\tau)^2} \tag{5}$$

$$\sigma_{yx}(\omega, \mu_c, \tau, T, B_0) = \sigma_0 \frac{\omega_c \tau}{(\omega_c \tau)^2 + (1 + j\omega\tau)^2} \tag{6}$$

with

$$\sigma_0 = \frac{e^2 \tau k_B T}{\pi \hbar^2} \left[\frac{\mu_c}{k_B T} + 2\ln\left(e^{-\mu_c/k_B T} + 1\right) \right] \tag{7}$$

where k_B is the Boltzmann constant, T is the Kelvin temperature ($T = 300$ K in this paper), $\hbar$ is the reduced Planck's constant, τ is the scattering time, and $\omega_c \approx eB_0 v_F^2/\mu_c$ is the cyclotron frequency with $v_F \approx 10^6$ m/s denoting the Fermi velocity.

By considering the graphene layer as an infinitesimal thin conductive sheet, the following boundary conditions over the graphene sheet have to be satisfied:

$$\hat{\mathbf{n}} \times (\mathbf{E}^+ - \mathbf{E}^-) = 0 \tag{8}$$

$$\hat{\mathbf{n}} \times (\mathbf{H}^+ - \mathbf{H}^-) = \overline{\overline{\sigma}}_g \cdot \mathbf{E} \tag{9}$$

where the superscripts $-$ and $+$ represent the two sides of the graphene sheet, $\hat{\mathbf{n}}$ is a unit vector pointing normal to the

resistive surface.

Since the incorporation of boundary conditions in DGTD is enforced by redefining the numerical flux, the anisotropic boundary condition in (9) definitely results in a tensor form flux expression and simultaneously dispersive, which no doubt complicates the problem significantly (The convolution in the time-domain is required and the different components of electromagnetic fields are entangled with each other). To address these toughes, an auxiliary polarization surface current $\mathbf{J}(\omega)$ is introduced by rewriting (9) as

$$\hat{\mathbf{n}} \times \left(\mathbf{H}^+ - \mathbf{H}^-\right) = \mathbf{J}(\omega) \tag{10}$$

with $\mathbf{J}$ governed by the ADE

$$J_x(\omega) = \sigma_{xx}E_x - \sigma_{yx}E_y \tag{11}$$
$$J_y(\omega) = \sigma_{yx}E_x + \sigma_{xx}E_y \tag{12}$$

After some mathematical manipulations, (11) and (12) can be rewritten as

$$j\omega J_x(\omega) = -2\Gamma J_x(\omega) - \omega_c J_y(\omega) + 2\Gamma\sigma_0 E_x(\omega) \tag{13}$$
$$j\omega J_y(\omega) = -2\Gamma J_y(\omega) + \omega_c J_x(\omega) + 2\Gamma\sigma_0 E_y(\omega) \tag{14}$$

where $\Gamma = \frac{1}{2\tau}$ denotes the phenomenological scattering rate.

Through the inverse Fourier transform, the time-domain counterparts of (13) and (14) can be obtained as

$$\frac{\partial \mathbf{J}}{\partial t} = \overline{\overline{\mathbf{C}}} \cdot \mathbf{J} + 2\Gamma\sigma_0 \mathbf{E} \tag{15}$$

with

$$\overline{\overline{\mathbf{C}}} = \left[\begin{array}{cc} -2\Gamma & -\omega_c \\ \omega_c & -2\Gamma \end{array}\right] \tag{16}$$

With this auxiliary polarization surface current $\mathbf{J}$ and the ADE in (15), the anisotropic and dispersive RBC in (9) is transformed to an isotropic and nondispersive one in (10). Then, the incorporation of this scalar RBC into DGTD can be facilitated in the conventional way by reformulating the numerical flux based on the *Rankine-Hugoniot jump relations* for Riemann problems.

For an arbitrary mesh element i (tetrahedrons are used in this paper), the jump relations along three different *characteristic curves* [17] for the f-th face of element i are defined as (assume face f_g of element i is over the graphene sheet):

1) Jump across the characteristic curve $\xi_n = -c^i t$

$$\frac{1}{\mu^i}\hat{\mathbf{n}}_{i,f} \times (\mathbf{E}_f^* - \mathbf{E}^i) = -c^i(\mathbf{H}_f^* - \mathbf{H}^i) \tag{17}$$

$$\frac{1}{\epsilon^i}\hat{\mathbf{n}}_{i,f} \times (\mathbf{H}^i - \mathbf{H}_f^*) = -c^i(\mathbf{E}_f^* - \mathbf{E}^i) \tag{18}$$

2) Jump across the characteristic curve $\xi_n = 0$

$$\hat{\mathbf{n}}_{i,f} \times (\mathbf{E}_f^{**} - \mathbf{E}_f^*) = 0 \tag{19}$$
$$\hat{\mathbf{n}}_{i,f} \times (\mathbf{H}_f^{**} - \mathbf{H}_f^*) = \alpha_g \mathbf{J} \tag{20}$$

3) Jump across the characteristic curve $\xi_n = c_f^j t$

$$\frac{1}{\mu_f^j}\hat{\mathbf{n}}_{i,f} \times (\mathbf{E}_f^j - \mathbf{E}_f^{**}) = c_f^j(\mathbf{H}_f^j - \mathbf{H}_f^{**}) \tag{21}$$

$$\frac{1}{\epsilon_f^j}\hat{\mathbf{n}}_{i,f} \times (\mathbf{H}_f^{**} - \mathbf{H}_f^j) = c_f^j(\mathbf{E}_f^j - \mathbf{E}_f^{**}) \tag{22}$$

where $1 \leq f \leq 4$ for the tetrahedron, j denotes the neighboring element sharing the f-face of element i, $\hat{\mathbf{n}}_{i,f}$ is the outward unit normal vector of face f. c^i and c_f^j represent the characteristic speed in element i and its neighboring j, respectively. $\epsilon^{i/j}$ and $\mu^{i/j}$ are the permittivity and permeability, respectively. $\left(\mathbf{E}_f^*, \mathbf{H}_f^*\right)$ and $\left(\mathbf{E}_f^{**}, \mathbf{H}_f^{**}\right)$ are the intermediate states in element i and j, respectively. It is noted that the incorporation of the RBC is facilitated by disrupting the tangential continuity of intermediate variables $\mathbf{H}_f^*$ and $\mathbf{H}_f^{**}$. The above jump relations have to be satisfied over the faces shared by element i and j. The parameter α_g is defined as

$$\alpha_g = \left\{\begin{array}{l} 1, \ f = f_g \\ 0, \ f \neq f_g \end{array}\right. \tag{23}$$

By combining (17), (19), (20), and (21), the upwind flux for the Ampere's law equation is formulated by

$$\hat{\mathbf{n}}_{i,f} \times \mathbf{H}_f^* = \hat{\mathbf{n}}_{i,f} \times \left[\frac{\left(Z^i\mathbf{H}^i + Z_f^j\mathbf{H}_f^j\right) + \hat{\mathbf{n}}_{i,f} \times \left(\mathbf{E}^i - \mathbf{E}_f^j\right)}{Z^i + Z_f^j}\right.$$

$$\left. +\alpha_g \frac{Z^j\mathbf{J}_{f_g}^i}{\left(Z^i + Z_f^j\right)}\right], \tag{24}$$

and by referring to (18), (19), (20) and (22), the upwind flux for the Maxwell-Faraday's law equation is given by

$$\hat{\mathbf{n}}_{i,f} \times \mathbf{E}_f^* = \hat{\mathbf{n}}_{i,f} \times \left[\frac{\left(Y^i\mathbf{E}^i + Y_f^j\mathbf{E}_f^j\right) + \hat{\mathbf{n}}_{i,f} \times \left(\mathbf{H}_f^j - \mathbf{H}^i\right)}{Y^i + Y_f^j}\right.$$

$$\left. -\alpha_g \frac{\mathbf{J}_{f_g}^i}{2\left(Y^i + Y_f^j\right)}\right], \tag{25}$$

where $Z^i = \sqrt{\mu^i/\epsilon^i}$ and $Z_f^j = \sqrt{\mu_f^j/\epsilon_f^j}$ represent the characteristic impedance of element i and the neighboring at the f-th face.

B. Formulation of DGTD

Let Ω denote the computation domain of interest, which is bound by surface $\partial\Omega$. With DGTD, the domain Ω is firstly split into N non-overlapping tetrahedrons Ω_i with boundary $\partial\Omega_i$. In element i, the electric field $\mathbf{E}$ and magnetic field $\mathbf{H}$ are approximated by 3-D vector basis functions $\Phi^i(\mathbf{r})$, $\Psi^i(\mathbf{r})$ [18], [26], and the polarization current $\mathbf{J}$ is approximated by 2-D vector basis functions $\varphi^i(\mathbf{r})$ (Without loss of generality, we assume that one of the element's faces is over the graphene

sheet):

$$\mathbf{E}^i = \sum_{k=1}^{n_e^i} e_k^i(t)\mathbf{\Phi}_k^i(\mathbf{r}) \tag{26}$$

$$\mathbf{H}^i = \sum_{l=1}^{n_h^i} h_k^i(t)\mathbf{\Psi}_l^i(\mathbf{r}) \tag{27}$$

$$\mathbf{J}^i = \sum_{q=1}^{n_c^i} c_q^i(t)\boldsymbol{\varphi}_q^i(\mathbf{r}) \tag{28}$$

where n_e^i, n_h^i, and n_c^i are the number of vector basis function for $\mathbf{E}$, $\mathbf{H}$, and $\mathbf{J}$ in i-th element, respectively; e_k^i, h_k^i, and c_q^i are the unknown time-dependent coefficients of basis functions $\Phi^i(\mathbf{r})$, $\Psi^i(\mathbf{r})$, and $\varphi^i(\mathbf{r})$.

By applying the DG testing over the two first-order time-derivative Maxwell's curl equations and the ADE in (15), we can obtain

$$\int_{\Omega_i} \mathbf{\Phi}_k^i \cdot \left[\epsilon_i \frac{\partial \mathbf{E}^i}{\partial t} - \nabla \times \mathbf{H}^i \right] d\mathbf{r} =$$
$$\sum_{f=1}^{4} \int_{\partial\Omega_{i,f}} \mathbf{\Phi}_k^i \cdot \left[\hat{\mathbf{n}}_{i,f} \times (\mathbf{H}_f^* - \mathbf{H}^i) \right] d\mathbf{r} \tag{29}$$

$$\int_{\Omega_i} \mathbf{\Psi}_l^i \cdot \left[\mu_i \frac{\partial \mathbf{H}^i}{\partial t} + \nabla \times \mathbf{E}^i \right] d\mathbf{r} =$$
$$\sum_{f=1}^{4} \int_{\partial\Omega_{i,f}} \mathbf{\Psi}_l^i \cdot \left[\hat{\mathbf{n}}_{i,f} \times (\mathbf{E}^i - \mathbf{E}_f^*) \right] d\mathbf{r} \tag{30}$$

$$\int_{\partial\Omega_{i,f_g}} \boldsymbol{\varphi}_q^i \cdot \frac{\partial \mathbf{J}^i}{\partial t} d\mathbf{r} = \int_{\partial\Omega_{i,f_g}} \boldsymbol{\varphi}_q^i \cdot \overline{\overline{\mathbf{C}}} \cdot \mathbf{J}^i d\mathbf{r} + 2\Gamma\sigma_0 \int_{\partial\Omega_{i,f_g}} \boldsymbol{\varphi}_q^i \cdot \mathbf{E}^i d\mathbf{r} \tag{31}$$

With (24)-(28), the semi-discrete matrix equations can be derived as:

$$\bar{\mathbf{M}}_e^i \frac{\partial \mathbf{e}^i}{\partial t} = \bar{\mathbf{S}}_e^i \mathbf{h}^i + \sum_{f=1}^{4} \left(\bar{\mathbf{F}}_{ee}^{ii,f} \mathbf{e}_f^i + \bar{\mathbf{F}}_{ee}^{ij,f} \mathbf{e}_f^j \right. \tag{32}$$
$$\left. + \bar{\mathbf{F}}_{eh}^{ii,f} \mathbf{h}_f^i + \bar{\mathbf{F}}_{eh}^{ij,f} \mathbf{h}_f^j \right) + \alpha_g \bar{\mathbf{F}}_{ec}^{ii,f_g} \mathbf{c}^i$$

$$\bar{\mathbf{M}}_h^i \frac{\partial \mathbf{h}^i}{\partial t} = -\bar{\mathbf{S}}_h^i \mathbf{e}^i + \sum_{f=1}^{4} \left(\bar{\mathbf{F}}_{hh}^{ii,f} \mathbf{h}_f^i + \bar{\mathbf{F}}_{hh}^{ij,f} \mathbf{h}_f^j \right. \tag{33}$$
$$\left. + \bar{\mathbf{F}}_{he}^{ii,f} \mathbf{e}_f^i + \bar{\mathbf{F}}_{he}^{ij,f} \mathbf{e}_f^j \right) + \alpha_g \bar{\mathbf{F}}_{he}^{ii,f_g} \mathbf{c}^i$$

$$\bar{\mathbf{J}}^i \frac{\partial \mathbf{c}^i}{\partial t} = \bar{\mathbf{M}}_c \mathbf{c}^i + 2\Gamma\sigma_0 \bar{\mathbf{M}}_v \mathbf{e}^i \tag{34}$$

where

$$\left[\bar{\mathbf{M}}_e^i \right]_{kl} = \int_{\Omega_i} \mathbf{\Phi}_k^i \cdot \epsilon^i \mathbf{\Phi}_l^i d\mathbf{r} \tag{35}$$

$$\left[\bar{\mathbf{M}}_h^i \right]_{kl} = \int_{\Omega_i} \mathbf{\Psi}_k^i \cdot \mu^i \mathbf{\Psi}_l^i d\mathbf{r} \tag{36}$$

$$\left[\bar{\mathbf{S}}_e^i \right]_{kl} = \int_{\Omega_i} \mathbf{\Phi}_k^i \cdot \nabla \times \mathbf{\Psi}_l^i d\mathbf{r} \tag{37}$$

$$\left[\bar{\mathbf{S}}_h^i \right]_{kl} = \int_{\Omega_i} \mathbf{\Psi}_k^i \cdot \nabla \times \mathbf{\Phi}_l^i d\mathbf{r} \tag{38}$$

$$\left[\bar{\mathbf{J}}^i \right]_{kl} = \int_{\partial\Omega_{i,f_g}} \boldsymbol{\varphi}_k^i \cdot \boldsymbol{\varphi}_l^i d\mathbf{r} \tag{39}$$

$$\left[\bar{\mathbf{M}}_c \right]_{kl} = \int_{\partial\Omega_{i,f_g}} \boldsymbol{\varphi}_k^i \cdot \overline{\overline{\mathbf{C}}} \cdot \boldsymbol{\varphi}_l^i d\mathbf{r} \tag{40}$$

$$\left[\bar{\mathbf{M}}_v \right]_{kl} = \int_{\partial\Omega_{i,f_g}} \boldsymbol{\varphi}_k^i \cdot \mathbf{\Phi}_l^i d\mathbf{r} \tag{41}$$

$$\left[\mathbf{F}_{ee}^{ii,f} \right]_{kl} = \frac{-1}{Z^i + Z_f^j} \int_{\partial\Omega_{i,f}} \mathbf{\Phi}_k^i \cdot \hat{\mathbf{n}}_{i,f} \times (\hat{\mathbf{n}}_{i,f} \times \Phi_l^i) d\mathbf{r} \tag{42}$$

$$\left[\bar{\mathbf{F}}_{ee}^{ij,f} \right]_{kl} = \frac{1}{Z^i + Z_f^j} \int_{\partial\Omega_{i,f}} \mathbf{\Phi}_k^i \cdot \hat{\mathbf{n}}_{i,f} \times (\hat{\mathbf{n}}_{i,f} \times \Phi_l^{j,f}) d\mathbf{r} \tag{43}$$

$$\left[\bar{\mathbf{F}}_{eh}^{ii,f} \right]_{kl} = -\frac{Z_f^j}{Z^i + Z_f^j} \int_{\partial\Omega_{i,f}} \mathbf{\Phi}_k^i \cdot \hat{\mathbf{n}}_{i,f} \times \mathbf{\Psi}_l^i d\mathbf{r} \tag{44}$$

$$\left[\bar{\mathbf{F}}_{eh}^{ij,f} \right]_{kl} = \frac{Z_f^j}{Z^i + Z_f^j} \int_{\partial\Omega_{i,f}} \mathbf{\Phi}_k^i \cdot \hat{\mathbf{n}}_{i,f} \times \mathbf{\Psi}_l^{j,f} d\mathbf{r} \tag{45}$$

$$\left[\bar{\mathbf{F}}_{ec}^{ii,f_g} \right]_{kl} = \frac{Z_{f_g}^j}{Z^i + Z_{f_g}^j} \int_{\partial\Omega_{i,f_g}} \mathbf{\Phi}^i \cdot \boldsymbol{\varphi}_l^i d\mathbf{r} \tag{46}$$

$$\left[\bar{\mathbf{F}}_{hh}^{ii,f} \right]_{kl} = \frac{-1}{Y^i + Y_f^j} \int_{\partial\Omega_{i,f}} \mathbf{\Psi}_k^i \cdot \hat{\mathbf{n}}_{i,f} \times (\hat{\mathbf{n}}_{i,f} \times \mathbf{\Psi}_l^i) d\mathbf{r} \tag{47}$$

$$\left[\bar{\mathbf{F}}_{hh}^{ij,f} \right]_{kl} = \frac{1}{Y^i + Y_f^j} \int_{\partial\Omega_{i,f}} \mathbf{\Psi}_k^i \cdot \hat{\mathbf{n}}_{i,f} \times (\hat{\mathbf{n}}_{i,f} \times \mathbf{\Psi}_l^{j,f}) d\mathbf{r} \tag{48}$$

$$\left[\bar{\mathbf{F}}_{he}^{ii,f} \right]_{kl} = \frac{Y_f^j}{Y^i + Y_f^j} \int_{\partial\Omega_{i,f}} \mathbf{\Psi}_k^i \cdot \hat{\mathbf{n}}_{i,f} \times \mathbf{\Phi}_l^i d\mathbf{r} \tag{49}$$

$$\left[\bar{\mathbf{F}}_{he}^{ij,f} \right]_{kl} = \frac{-Y_f^j}{Y^i + Y_f^j} \int_{\partial\Omega_{i,f}} \mathbf{\Psi}_k^i \cdot \hat{\mathbf{n}}_{i,f} \times \mathbf{\Phi}_l^{j,f} d\mathbf{r} \tag{50}$$

$$\left[\bar{\mathbf{F}}_{he}^{ii,f_g} \right]_{kl} = \frac{1}{Y^i + Y_{f_g}^j} \int_{\partial\Omega_{i,f_g}} \mathbf{\Psi}_k^i \cdot (\hat{\mathbf{n}}_{i,f_g} \times \boldsymbol{\varphi}_l^i) d\mathbf{r} \tag{51}$$

In this work, 12 edge vector basis functions (six constant tangential/linear normal (CT/LN) and six linear tangential/linear normal (LT/LN) basis functions, respectively) are used for both $\mathbf{E}$ and $\mathbf{H}$ in each mesh element, i.e., $n_e^i = 12$ and $n_h^i = 12$ for $i = 1, \cdots, N$. Since the surface polarization current $\mathbf{J}^i$ has only tangential components, thus its basis function $\boldsymbol{\varphi}^i(\mathbf{r})$ actually can be constructed by $\hat{\mathbf{n}}_{i,f_g} \times \Phi^i(\mathbf{r}) \times \hat{\mathbf{n}}_{i,f_g}$ based on the property of the edge vector basis function. Consequently, the number of basis functions for the auxiliary surface current $\mathbf{J}$ is 6 since each face has only 6 basis functions with non-zero tangential components.

To solve the semi-discrete matrix equations from (32) to (34), the fourth-order RK method is employed. For explicit time-marching scheme, the Courant-Friedrichs-Lewy (CFL)-like condition must be satisfied to ensure stability. In general, the time step size δt is determined in terms of the following condition [19], [23], [24]:

$$c_0 \delta t \leq \min\{l_{min}\sqrt{\epsilon_r \mu_r}/4(p+1)^2\} \tag{52}$$

where c_0 is the free-space light speed, p is the order of basis function. In this work, first-order basis functions are used, thus $p = 1$.
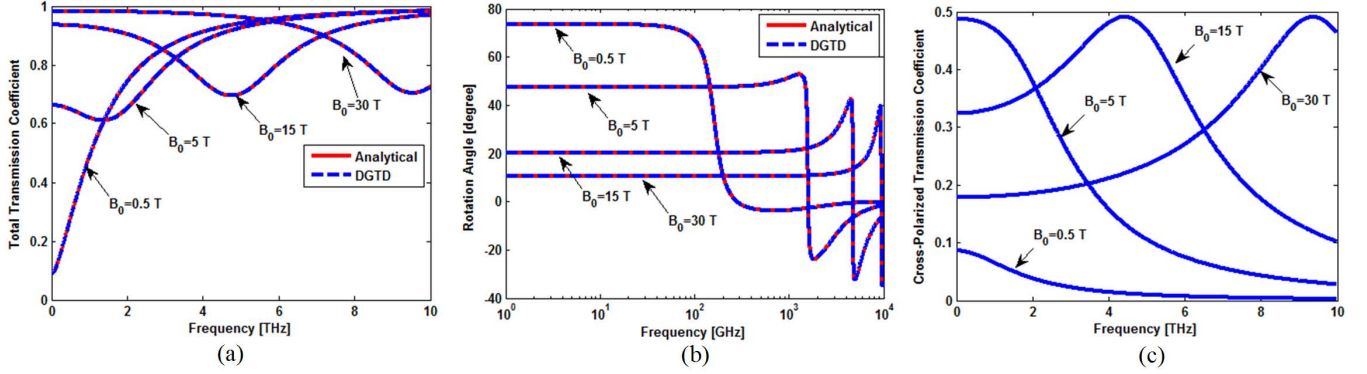
Fig. 1. The total transmission coefficients (a), Faraday rotation angle (b), and the cross-polarized transmission coefficients (c) versus frequency for different magnetostatic biasing.
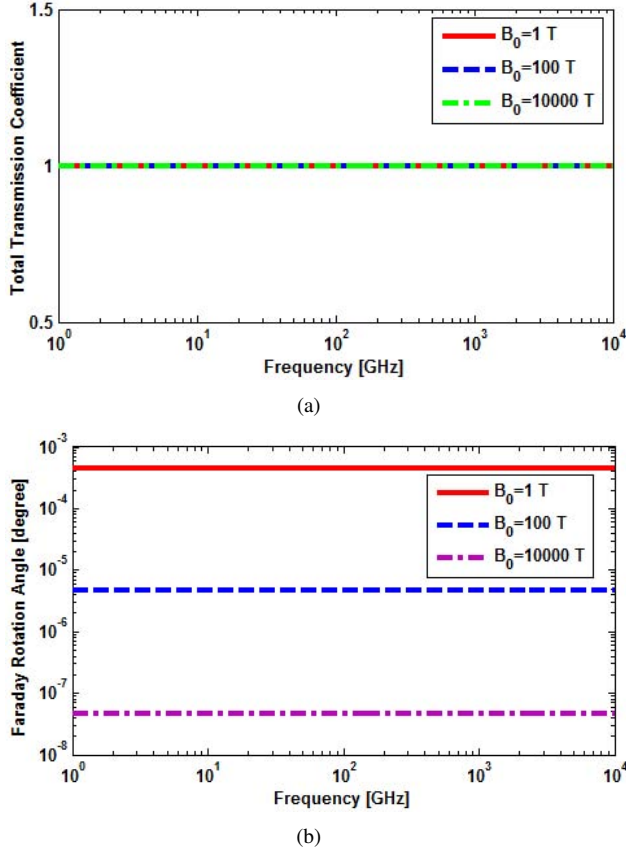

Fig. 2. The total transmission coefficient (a) and the Faraday rotation angle θ_F for different magnetic biasing when $\mu_c = 10^{-5}$ eV.

C. TDBI Formulation

The field values $\mathbf{E}_f^j$ and $\mathbf{H}_f^j$ over the computational boundary $\partial\Omega$ used for computing the incoming numerical flux in (24) and (25) are evaluated by the TDBI method on the basis of Huygens' principle. Let the Huygens' surface $\partial\Gamma$ be discretized by triangular facets $\partial\Omega_{i',m'}$, where i' runs over the indices of elements that are outside the volume enclosed by $\partial\Gamma$ and have at least three nodes residing on $\partial\Gamma$, and f' runs over the indices of each element's facets that are described by these nodes. On the surface mesh described by $\partial\Omega_{i',f'}$, one can introduce (equivalent) electric and magnetic surface

currents, $\mathbf{J}_{i',f'}^{\mathrm{h}}(\mathbf{r},t)$ and $\mathbf{J}_{i',f'}^{\mathrm{e}}(\mathbf{r},t)$ [?], [25]:

$$\mathbf{J}_{i',f'}^{\mathrm{h}}(\mathbf{r},t) = \sum_{l'=1}^{n_h^{i'}} h_{i',l'}(t)\hat{\mathbf{n}}_{i',f'}(\mathbf{r}) \times \boldsymbol{\Psi}_{i',l'}(\mathbf{r}) \quad (53)$$

$$\mathbf{J}_{i',f'}^{\mathrm{e}}(\mathbf{r},t) = -\sum_{k'=1}^{n_e^{i'}} e_{i',k'}(t)\hat{\mathbf{n}}_{i',f'}(\mathbf{r}) \times \boldsymbol{\Phi}_{i',k'}(\mathbf{r})$$

The boundary fields $\mathbf{E}_f^{j,\partial\Omega}$ and $\mathbf{H}_f^{j,\partial\Omega}$ are then constructed using currents $\mathbf{J}_{i',m'}^{\mathrm{h}}$ and $\mathbf{J}_{i',m'}^{\mathrm{e}}$ [25], [27], [28]:

$$\mathbf{E}_f^{j,\partial\Omega}(\mathbf{r},t) = \sum_{i'}\sum_{f'}[\mu_0\mathcal{L}_{i',f'}(\mathbf{J}_{i',f'}^{\mathrm{h}}) - \mathcal{K}_{i',f'}(\mathbf{J}_{i',f'}^{\mathrm{e}})] \quad (54)$$

$$\mathbf{H}_f^{j,\partial\Omega}(\mathbf{r},t) = \sum_{i'}\sum_{f'}[\epsilon_0\mathcal{L}_{i',f'}(\mathbf{J}_{i',f'}^{\mathrm{e}}) + \mathcal{K}_{i',f'}(\mathbf{J}_{i',f'}^{\mathrm{h}})].$$

Here, the operators $\mathcal{L}_{i',f'}$ and $\mathcal{K}_{i',f'}$ are defined as

$$\mathcal{L}_{i',f'}(\mathbf{J}) = -\frac{1}{4\pi}\int_{\partial\Omega_{i',f'}}\frac{\partial_t\mathbf{J}(\mathbf{r}',t-R/c)}{R}d\mathbf{r}'$$

$$+ \frac{c^2}{4\pi}\nabla\int_{\partial\Omega_{i',f'}}\int_0^{t-R/c}\frac{\nabla'\cdot\mathbf{J}(\mathbf{r}',t')}{R}dt'd\mathbf{r}' \quad (55)$$

$$\mathcal{K}_{i',f'}(\mathbf{J}) = \frac{1}{4\pi}\nabla\times\int_{\partial\Omega_{i',f'}}\frac{\mathbf{J}(\mathbf{r}',t-R/c)}{R}d\mathbf{r}'$$

where $R = |\mathbf{r}-\mathbf{r}'|$ is the distance between the integration point $\mathbf{r}' \in \partial\Omega_{i',m'}$ and the observation point $\mathbf{r}$ and $c = 1/\sqrt{\epsilon\mu}$ is the speed of light in the background medium.

To discretize the $\mathcal{L}$ and $\mathcal{K}$ operators in (55), a linear shifted interpolation function is employed as the temporal basis functions [26]. Since the different time-step sizes of DGTD and TDBI, interpolations are required for field values at the truncation boundary and the Huygens' surface, where the incoming flux evaluation required fields at the truncation boundary are calculated by TDBI with time step size δt_{BI} [see (54)] while the equivalent currents required fields [see (53)] at the Huygens' surface are computed by DGTD with time step size δt_{DG} [see (32) and (33)].

III. NUMERICAL RESULTS

To validate and demonstrate the accuracy of this proposed algorithm, the Faraday rotation and surface plasmon polarization are studied by varying the chemical potential μ_c and the magnetostatic biasing $\mathbf{B}_0$.
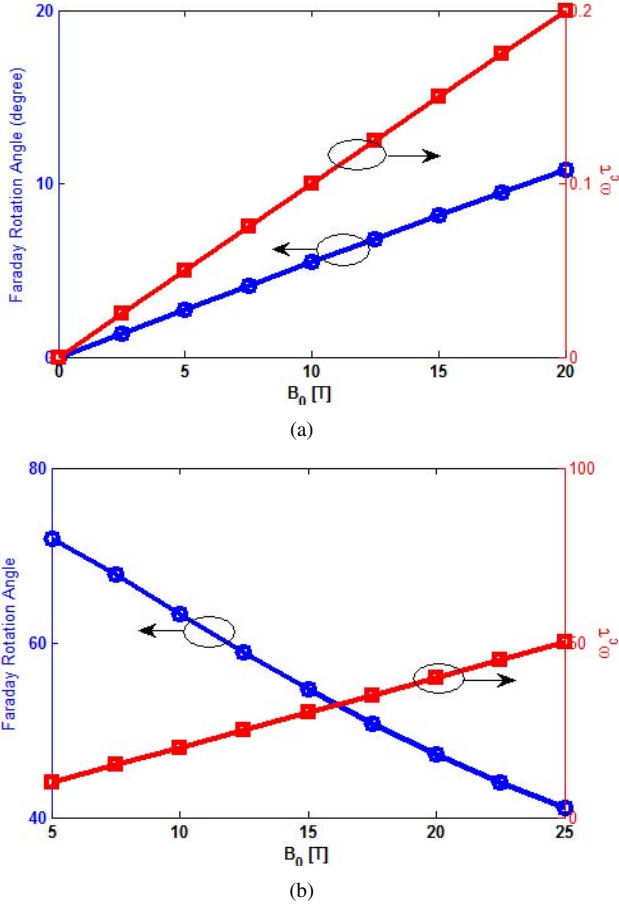
(a)

(b)

Fig. 3. The Faraday rotation angle θ_F as a function of static magnetic field biasing in the range $\omega_c\tau \ll 1$ (a) and $\omega_c\tau \gg 1$ (b).

A. An Infinitely Large Graphene Sheet

For the first example, an infinitely large graphene sheet placed at xy plane is biased by a z-directed magnetostatic field $\mathbf{B}_0 = \hat{z}B_0$. For the excitation, a plane wave defined as $\mathbf{E}^{\text{inc}}(\mathbf{r},t) = \hat{x}g(t - \hat{\mathbf{k}}\cdot\mathbf{r}/c_0)$ is used, where $\hat{\mathbf{k}} = \hat{z}$ is the direction of propagation, $g(t) = \exp(-[t-t_0]^2/\tau_m^2)\cos(2\pi f_m[t-t_0])$ is a Gaussian pulse with modulation frequency $f_m = 5$ THz, duration $\tau_m = 6.37 \times 10^{-13}$ s, and delay $t_0 = 5t_m$. The first-order Silver-Müller absorbing boundary condition (SM-ABC) [29] are employed to truncate the computational domain in the z direction, which is sufficient for this example since all incoming waves are normal to the boundary.

Firstly, we let $\mu_c = 0.5$ eV and the scattering time $\tau = 5 \times 10^{-12}$ s while varying the magnetic biasing B_0 from 0.5 to 30 T. In Fig. 1, the total transmission coefficient

$$T_{tot} = \frac{\sqrt{||E_{x,\text{obs}}(\omega)||^2 + ||E_{y,\text{obs}}(\omega)||}}{||E_{inc}(\omega)||}, \tag{56}$$

the Faraday rotation angle

$$\theta_F = \tan^{-1}\left(\frac{E_{y,\text{obs}}(\omega)}{E_{x,\text{obs}}(\omega)}\right), \tag{57}$$

and the cross-polarized transmission coefficient

$$T_{cross} = \frac{||E_{y,\text{obs}}(\omega)||}{||E_{inc}(\omega)||} \tag{58}$$
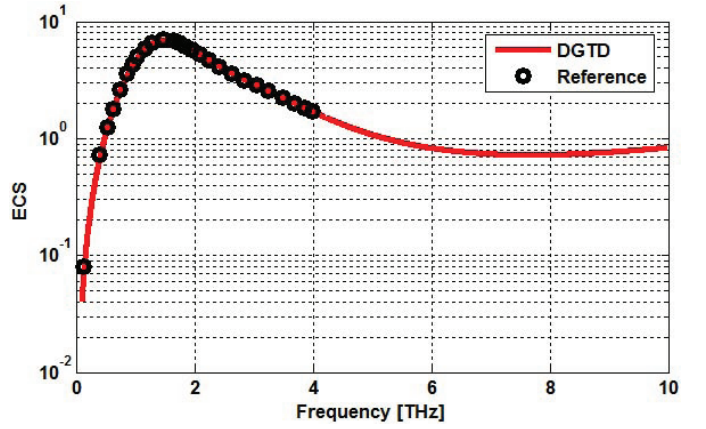

Fig. 4. The calculated extinction-cross-section (ECS) by the proposed DGTD-RBC algorithm and the reference result by integral equation method in [30]

are presented. For comparison, the analytical total transmission coefficient [7], [16]

$$T_{tot,\text{ana}} = \frac{2\sqrt{||2 + \sigma_{xx}\eta_0||^2 + ||\sigma_{yx}\eta_0||^2}}{||(2 + \sigma_{yx}\eta_0)^2 + (\sigma_o\eta_0)^2||} \tag{59}$$

and the analytical Faraday rotation angle [7]

$$\theta_{F,\text{ana}} = \tan^{-1}\left(\frac{\eta_0\sigma_{yx}}{2 + \eta_0\sigma_{xx}}\right) \tag{60}$$

are also provided. Very good agreements between the numerical results and the analytical ones are observed. The results show that the magnetostatic biasing has significant impacts on the electromagnetic waves propagating through a graphene sheet.

With regarding to the μ_c dependence, there is an interesting comment in [7] that for any value of B_0, the Faraday rotation angle $\theta_F \to 0$ when $\mu_c \to 0$. This is attributable to the fact that the conductivity of graphene is very small under this circumstance (only a very small amount of electrons exist in the conduction band). As a result, the interaction between the electromagnetic wave and the graphene is negligible. Therefore, the transmission coefficient $T_{tot} \to 1$ while $\theta_F \to 0$. To prove this assertion, we set $\mu_c = 10^{-5}$ eV and vary B_0 from 1 to 10^4 T. The calculated results are shown in Fig. 2 (a) and 2 (b), which agrees with the previous assertion. Similarly, the transmission coefficient $T_{tot} \to 0$ and $\theta_F \to 0$ when $\mu_c \to \infty$. This is because the conductivity of the graphene is very large in this case, thus acting as a perfect electrical conductor (PEC).

As for the B_0 dependence, there is also an interesting comment in [7] claiming that the Faraday rotation angle θ_F increases with B_0 in the range B_0 such that $\omega_c\tau \ll 1$, while θ_F decreases with B_0 in the range B_0 such that $\omega_c\tau \gg 1$. Firstly, the case $\omega_c\tau \ll 1$ is studied by setting $\tau = 10^{-13}$ s and $\mu_c = 10$ eV, the Faraday rotation angle θ_F at $f = 30$ GHz as the function of B_0 are presented in Fig. 3 (a). It is clearly observed that θ_F increases with B_0 in the range $\omega_c\tau \ll 1$. Next, the case $\omega_c\tau \gg 1$ is investigated by letting $\tau = 2 \times 10^{-12}$ s and $\mu_c = 1.0$ eV. In Fig. 3 (b), the Faraday rotation angle versus the magnetostatic biasing b_0 are
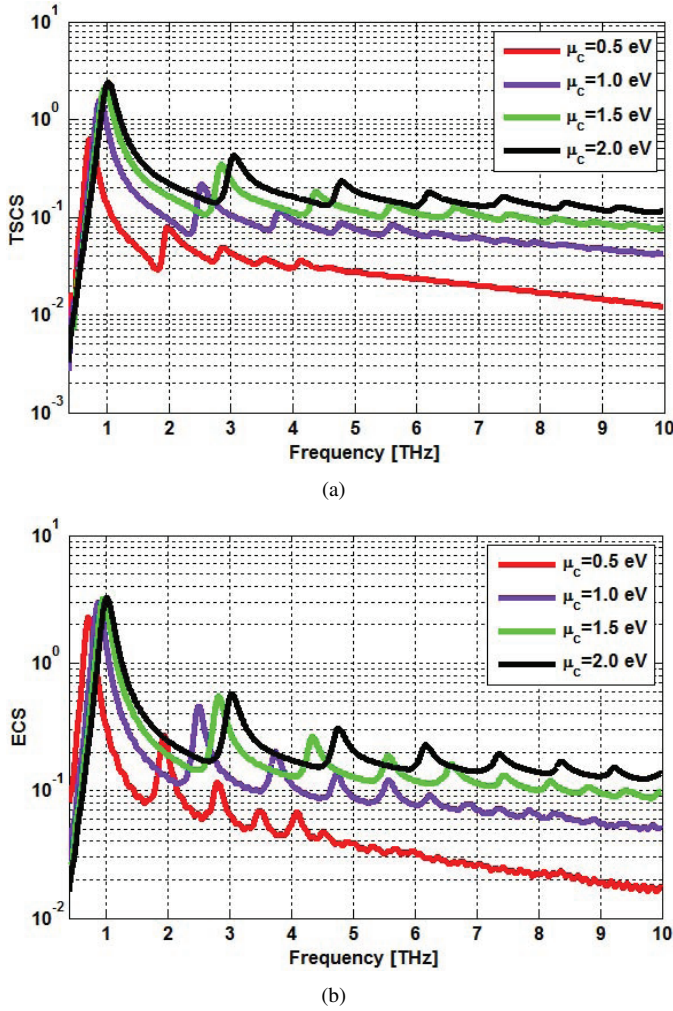
(a)

(b)

Fig. 5. The normalized total scattering-cross-section (TSCS) (a) and extinction-cross-section (ECS) (b) versus different chemical potentials.

presented. It is found that θ_F decreases with B_0 in the range $\omega_c \tau \gg 1$. This phenomenon is also observed in Fig. 2 (b).

B. Finite Size Graphene Patches

To validate the accuracy of the proposed algorithm for 3-D examples, a 5 by 10 μm unmagnetized graphene patch in [30] is revisited. The parameters of the surface conductivity σ_g are given by $T = 300$ K, $\mu_c = 0$ eV, and $\Gamma = \frac{1}{2\tau}$ with $\tau = 10^{-13}$ s. For convenience, the same plane wave in the first example is employed as the excitation. To rigorously truncate the computational domain, the hybrid DGTD and TDBI algorithm is applied. The time step sizes for DGTD and TDBI are 9.92×10^{-17} s and 1.97×10^{-15} s, respectively. For finite size geometries, the figure-of-merits of interest are the total-scattering cross-section (TSCS), the absorption cross-section (ACS), or the extinction cross-section (ECS). In Fig. 4, the calculated ECS and the reference by integral equation (IE) method [30] is also provided for comparison. It is noted that very good agreements are achieved.

Next, a 20 by 100 μm^2 graphene patch biased by a z-directed static magnetic field $\mathbf{B}_0 = 0.25\hat{z}$ is characterized. The graphene patch is illuminated by the same plane wave
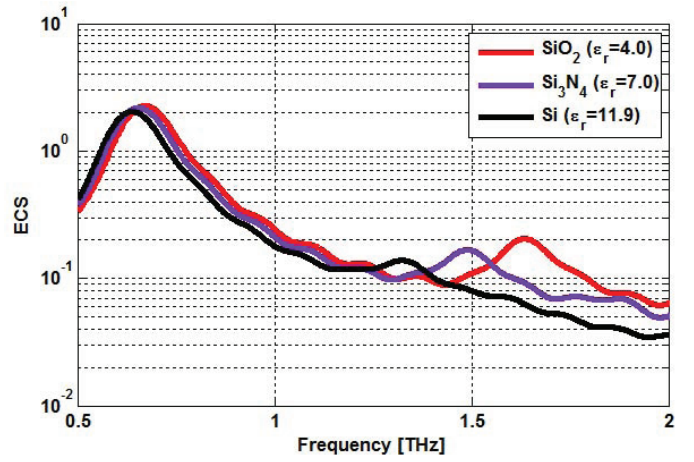

Fig. 6. The normalized extinction-cross-section (ECS) for substrates Si, SiO$_2$, and Si$_3$N$_4$.

as above and the hybrid DGTD-BI is applied to truncate the computational domain. The time step sizes of DGTD and TDBI are 1.1068×10^{-16} s and 2.6919×10^{-15} s, respectively; and the total number of tetrahedrons involved in this example is $102,758$. Firstly, to show the impacts of chemical potentials on the plasmon resonance, the TSCS and ECS corresponding to different μ_c are calculated by letting the scattering rate $\Gamma = 2.5$ meV/$\hbar$. The results are presented in Fig. 5. It is noted that the resonant frequencies shift upwards with higher chemical potentials, and the resonance becomes more stronger.

Secondly, to study the influences of substrates on the plasmon resonance, the graphene patch is supposed to be covered by different mediums with thickness $h = 2$ μm. They are silicon (Si), silicon-nitrate (Si$_3$N$_4$), and silicon-dioxide (SiO$_2$), which are commonly used by experimental researchers. The calculated ECS with $\mu_c = 0.5$ eV is shown in Fig. 6. It is noted that the first two resonant peaks of the ECS shifts to low frequencies with the increasing of permittivity. This is due to that the physical dimension of the graphene becomes larger compared with wavelength $\lambda = \lambda_0 / \sqrt{\epsilon_r}$.

C. A Graphene-Strip Grating

In the last example, a grating structure composed of three graphene strips placed in the $z = 0$ plane with a static magnetic biasing $\hat{\mathbf{B}}_0 = B_0\hat{z}$ is investigated. This grating structure has three x-directed graphene strips but periodically placed along the y-axis with periodicity $p = 15$ μm. Each of the strips has width $w = 10$ μm and length $l = 50$ μm. The same plane wave excitation as the above examples is applied again. Furthermore, the hybrid DGTD and TDBI method is used [26]. For this simulation, the chemical potential μ_c and scattering rate Γ are set to be 1.0 eV and 2.5 meV/$\hbar$, respectively. The number of tetrahedrons is $80,425$, the time step size δt_{DG} for DGTD and δt_{BI} for TDBI are 1.01×10^{-16} s and 2.17×10^{-15} s, respectively.

Firstly, the TSCS and ACS corresponding to different magnetic biasing are calculated, as shown in Fig. 7. As can be seen, the TSCS and ACS display sharp maxima at some frequency points in the terahertz band, which are due to the far
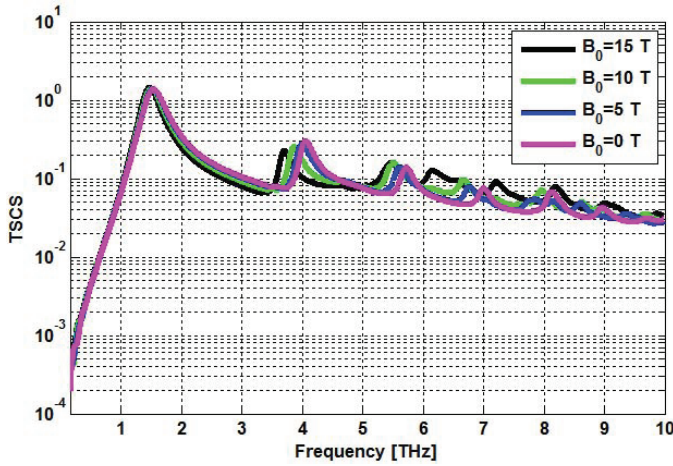
(a)
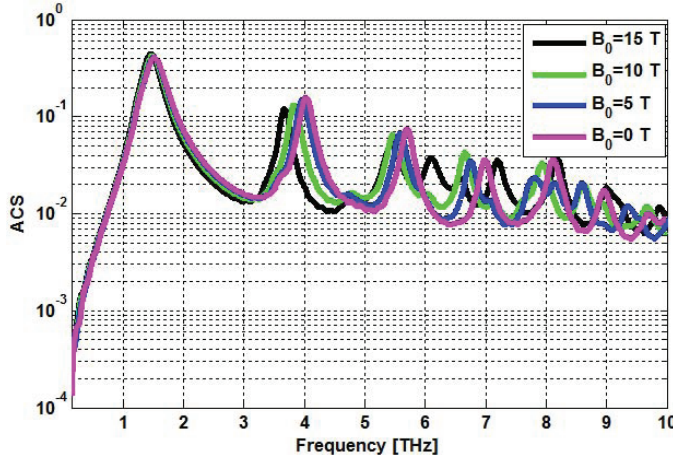
(b)

Fig. 7. The normalized TSCS (a) and ACS (b) versus different magnetostatic biasing from 0.1 THz to 10 THz.

and near field enhancement resulted from the surface-plasmon resonances. Next, to have a better insight into the surface plasmon polarization, the total electric near-fields over the plane where graphene residing are presented at $f_1 = 1.529$ THz, $f_2 = 4.003$ THz, and $f_3 = 5.628$ THz for $B_0 = 5$ T, as shown in Fig. 8. The near-field enhancement is obviously noted at these three plasmon resonance frequencies.

IV. CONCLUSION

In this paper, a DGTD based algorithm is developed to model the graphene biased by an external static magnetic field. To avoid very fine mesh cells, a tensor-form RBC is firstly applied over the graphene by regarding the graphene as an infinitesimal thin conductive sheet with an anisotropic surface conductivity $\overline{\overline{\sigma}}_g$ derived from the Kubo formula. By introducing an auxiliary polarization current $\mathbf{J}$ and an ADE over the graphene sheet, the dispersive anisotropic boundary condition is transformed into an isotropic and nondispersive one. This newly obtained RBC can be readily incorporated into DGTD by changing the jump relation along the characteristic curve. The accuracy and applicability of the proposed algorithm are verified by studying the transmission, cross-
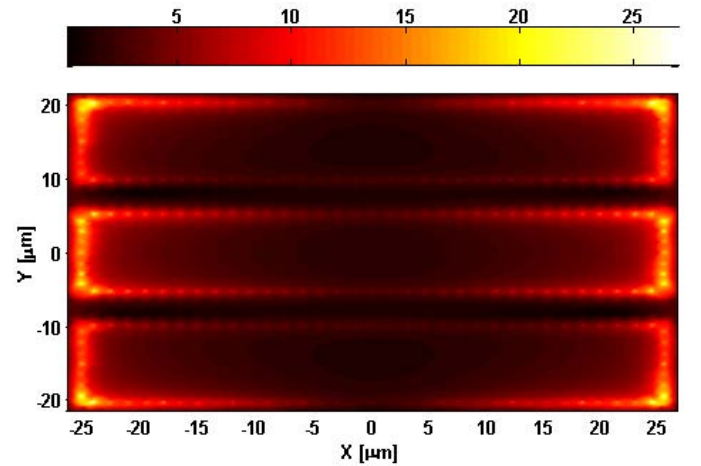
(a)
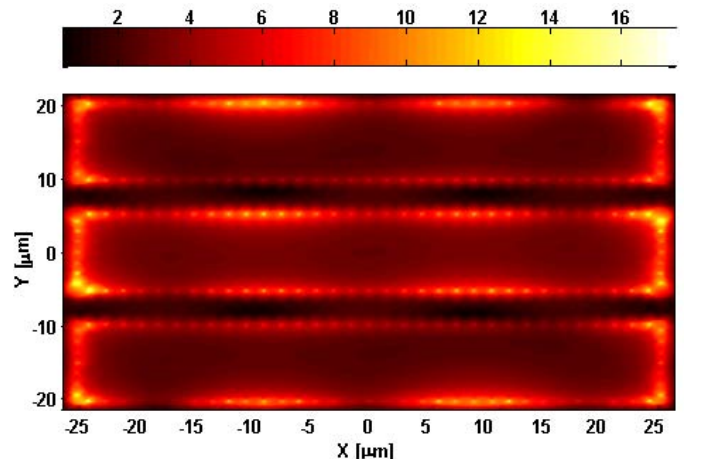
(b)
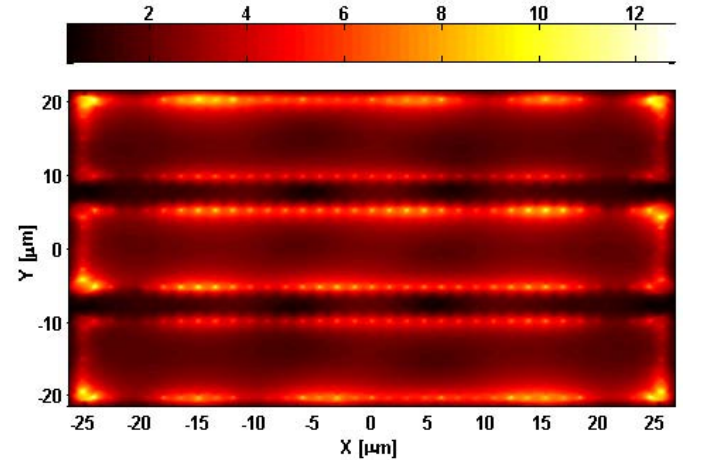
(c)

Fig. 8. The normalized electric near-field at $f_1 = 1.529$ THz (a), $f_2 = 4.003$ THz, and $f_3 = 5.618$ THz (c).

polarization, Faraday rotation, and plasmon resonance in the case of a graphene sheet illuminated by a plane wave.

REFERENCES

[1] A. K. Geim and K. S. Novoselov, "The rise of graphene," *Natural Mater.*, vol. 6, pp. 183-191, Mar. 2007.

[2] F. Schwierz, "Graphene transistors," *Nature Nanotechn.*, vol. 5, pp. 487-496, May 2010.

[3] M. Tamagnone, J. S. Gomez-Diaz, J. R. Mosig, and J. P. Carrier, "Analysis and design of terahertz antennas based on plasmonic resonant graphene sheets," *Appl. Phys. Lett.*, vol. 101, no. 214102, pp. 1-4, 2012.

[4] F. H. L. Koppens, D. E. Chang, and F. J. G. Abajo, "Graphene plasmonics: a platform for strong light-matter interactions," *Nano Lett.*, vol. 11, pp. 3370-3377, Jul. 2011.

[5] G. Lovat, "Equivalent circuit for electromagnetic interaction and transmission through graphene sheets," *IEEE Trans. Electromagn. Compat.*, vol. 54, no. 1, pp. 101-109, Feb. 2012.

[6] I. Crassee, J. Levallois, A. L. Walter, M. Ostler, A. Bostwick, E. Rotenberg, T. Seyller, D. Marel, and A. B. Kuzmenko, "Giant faraday rotation in single- and multilayer graphene," *Nature Phys.*, vol. 7, pp. 48-51, Jan. 2011.

[7] D. L. Sounas and C. Caloz, "Gyrotropy and nonreciprocity of graphene for microwave applications," *IEEE Trans. Microw. Theory Tech.*, vol. 60, no. 4, pp. 901-914, Apr. 2012.

[8] N. Chamanara, D. Sounas, and C. Caloz, "Non-reciprocal magnetoplasmon graphene coupler," *Opt. Express*, vol. 21, no. 9, pp. 11248-11256, May 2013.

[9] G. W. Hanson, "Dyadic Green's functions for an anisotropic, non-local model of biased graphene," *IEEE Trans. Antennas Propag.*, vol. 56, no. 3, pp. 747-757, Mar. 2008.

[10] O. V. Shapoval, J. S. G-Diaz, J. P-Carrier, J. R. Mosig, and A. I. Nosich, "Integral equation analysis of plane wave scattering by coplanar graphene-strip gratings in the THz range," *IEEE Trans. Terahertz Sci. Techn.*, vol. 6, no. 3, pp. 666-674, Sept. 2013.

[11] V. Nayyeri, M. Soleimani, and M. Ramahi, "Wideband modeling of graphene using the finite-difference time-domain metod," *IEEE Trans. Antennas Propag.*, vol. 6, no. 12, pp. 6107-6114, Dec. 2013.

[12] V. Nayyeri, M. Soleimani, and M. Ramahi, "Modeling graphene in the finite-difference time-domain method using a surface boundary condition," *IEEE Trans. Antennas Propag.*, vol. 6, no. 8, pp. 4176-4182, Aug. 2013.

[13] P. Li, L. J. Jiang, and H. Bagci, "A resistive boundary condition enhanced DGTD scheme for the transient analysis of graphene," *IEEE Trans. Antennas Propag.*, vol. 63, no. 7, pp. 1-12, Jul. 2015.

[14] H. Lin, M. F. Pantoja, L. D. Angulo, J. Alvarez, R. G. Martin, and S. G. Garcia, "FDTD modeling of graphene devices using complex conjugate dispersion material model," *IEEE Microw. Wireless Compon. Lett.*, vol. 22, no. 12, pp. 612-614, Dec. 2012.

[15] I. Ahmed, E. H. Khoo, and E. Li, "Efficient modeling and simulation of graphene devices with the LOD-FDTD method," *IEEE Microw. Wireless Compon. Lett.*, vol. 23, no. 6, pp. 306-308, Jun. 2013.

[16] X. H. Wang, W. Y. Yin, and Z. Chen, "Matrix Exponential FDTD Modeling of Magnetized Graphene Sheet," *IEEE Antennas Wireless Propag. Lett.*, vol. 12, pp. 1129-1132, Dec. 2013.

[17] K. Sankaran, "Accurate domian truncation techniques for time-domain conformal methods," Ph.D. dissertation, Dept. Inform. Technol. Elect. Eng., ETH Zurich, Zurich, Switzerland, 2007.

[18] P. Li and L. J. Jiang, "Integration of arbitrary lumped multiport circuit networks into discontinuous Galerkin time-domain analysis," *IEEE Trans. Microw. Theory and Tech.*, vol. 61, no. 7, pp. 2525-2534, Jul. 2013.

[19] P. Li and L. J. Jiang, "A hybrid electromagnetics-circuit simulation method exploiting discontinuous Galerkin finite element time domain method," *IEEE Microw. Wireless Compon. Lett.*, vol. 23, no. 3, pp. 113-115, Mar. 2013.

[20] P. Li, L. J. Jiang, and H. Bagci, "Co-simulation of electromagneticsC-circuit systems exploiting DGTD and MNA," *IEEE Trans. Components, Packaging, Manufacturing and Techn.*, vol. 4, no. 6, pp. 1052-1061, Jun. 2014.

[21] J. M. Jin, *The Finite Element Method in Electromagnetics*, 2nd ed. New York, USA: Wiley, 2003.

[22] R. Kubo, "Statistical-mechanical theory of irreversible processes. i. general theory and simple applications to magnetic and conduction problems," *J. Phys. Soc. Japan*, vol. 12, no. 6, pp. 570-586, 1957.

[23] P. Li and L. J. Jiang, "Simulation of electromagnetic waves in the magnetized cold plasma by a DGFETD method," *IEEE Antennas Wireless Propag. Lett.*, vol. 12, pp. 1244-1247, Dec. 2013.

[24] S. D. Gedney, C. Luo, J. A. Roden, R. D. Crawford, B. Guernsey, J. A. Miller, T. Kramer, and E. W. Lucas, "The discontinuous Galerkin finiteelement time-domain method solution of Maxwell's equations," *J. Appl. Comput. Electromagn. Society*, vol. 24, no. 2, pp. 129-142, Apr. 2009.

[25] D. Jiao, A. A. Ergin, B. Shanker, E. Michielssen, and J. M. Jin, "A fast higher-order time-domain finite element-boundary integral method for 3-D electromagnetic scattering analysis," *IEEE Trans. Antennas Propag.*, vol. 50, no. 9, pp. 1192-1202, Sept. 2002.

[26] P. Li, Y. Shi, L. J. Jiang, and H. Bagci, "A hybrid time-domain discontinuous galerkin-boundary integral method for electromagnetic scattering analysis," *IEEE Trans. Antennas Propag.*, vol. 62, no. 5, pp. 2841-2846, May 2014.

[27] P. Li and L. J. Jiang, "The far field transformation for the antenna modeling based on spherical electric field measurements," *Progress In Electromagnetics Research*, vol. 123, pp. 243-261, 2012.

[28] P. Li, Y. Li, L. J. Jiang, and J. Hu, "A wide-band equivalent source reconstruction method exploiting the stoer-bulirsch algorithm with the adaptive frequency sampling," *IEEE Trans. Antennas Propag.*, vol. 61, no. 10, pp. 5338-5343, Oct. 2013.

[29] S. Dosopoulos, B. Zhao, and J. F. Lee, "Non-conformal and parallel discontinuous Galerkin time domain method for Maxwell's equations: EM analysis of IC packages," *J. Comput. Phys.*, vol. 238, no. 12, pp. 48-70, Dec. 2012.

[30] I. Llatser, C. Kremers, A. C.-Aparicio, J. M. Jornet, E. Alarcon, and D. N. Chigrin, "Graphene-based nano-patch antenna for terahertz radiation," *Photonics Nanostructures: Fundamentals and Applications*, vol. 10, pp. 353-358, May 2012.

Ping Li (S'12-M'15) has been working toward the Ph.D. degree with the center of Electromagnetics and Optics at the University of Hong Kong since 2010. He is the recipient of the Postgraduate Engineering Fellowship from 2010. He is listed in Marquis Who's Who in the World, 32nd Edition, 2015.

He has authored over 10 journal papers on IEEE Trans. Microwave Theory and Techniques, IEEE Trans. Antennas and Propagation, IEEE Trans. Electromagnetic and Compatibility, IEEE Trans. Components, Packaging, and Manufacturing Technologies, etc. His paper was selected as the Finalist paper in 29-th International Review of Progress in Applied Computational Electromagnetics and 2014 International Symposium on Electromagnetic Compatibility, and he won the best student paper award in 12-th International Workshop on Finite Elements for Microwave Engineering. He served as the reviewer of IEEE Trans. Antennas and Propagation, IEEE Antennas and Wireless Propagation Letters, Proceedings of IEEE, and ACES Journal.

His research interests include the near-field to far-field transformation techniques, phaseless equivalent source reconstruction methods, discontinuous Galerkin time-domain method, and uncertainty quantification for large scale electromagnetic systems.

Li Jun Jiang (S'01-M'04-S'13) received the B.S. degree in Electrical Engineering from the Beijing University of Aeronautics and Astronautics in 1993, the M.S. degree in Electronic Engineering from the Tsinghua University in 1996, and P.h.D in Electrical and Computer Engineering from the University of Illinois at Urbana-Champaign in 2004. From 1996 to 1999, he was an application engineer with the Hewlett-Packard Company. Since 2004, he has been the postdoctoral researcher, the research staff member, and the senior engineer at IBM T.J. Watson Research Center. Since the end of 2009, he is an Associate Professor with the Department of Electrical and Electronic Engineering at the University of Hong Kong.

He received the IEEE MTT Graduate Fellowship Award in 2003 and the Y.T. Lo Outstanding Research Award in 2004. He is an IEEE Senior Member, the Associate Editor of IEEE Transactions on Antennas and Propagation, the Associate Editor of Progress in Electromagnetics Research, the Associate Guest Editor of the Proceedings of IEEE Special Issue in 2011 2012, an IEEE AP-S Member, an IEEE MTT-S member, an IEEE EMC-S member, an ACES member, and a member of Chinese Computational Electromagnetics Society. He was the Semiconductor Research Cooperation (SRC) Industrial Liaison for several academic projects. He served as the Scientific Consultant to Hong Kong ASTRI (Hong Kong Applied Science and Technology Research Institute Company Limited) in 2010-2011, the Panelist of the Expert Review Panel (ERP) of Hong Kong R&D Centre for Logistics and Supply Chain Management Enabling Technologies since Jan. 1st, 2013. He is also the senior visiting professor at Tsinghua University since Jun. 2013.

He was the TPC Chair of the 7th International Conference on Nanophotonics (ICNP)/the 3rd Conference on Advances in Optoelectronics and Micro/Nano Optics (AOM), the TPC Co-chair of the 12th International Workshop on Finite Elements for Microwave Engineering, the Co-chair of 2013 International Workshop on Pulsed Electromagnetic Field at Delft, the Netherlands, the General Chair of 2014 IEEE 14th HK AP/MTT Postgraduate Conference. He was the elected TPC member of IEEE EPEP since 2014, the TPC member of IEEE EDAPS since 2010, the TPC member of 2013 IEEE ICMTCE, the scientific committee member of 2010 IEEE SMEE, the special session organizers of IEEE EDAPS, IEEE EMC, ACES, AP-RASC, PIERS, co-organizer of HKU Computational Science and Engineering Workshops in 2010-2012, the TC-9 and TC-10 member of IEEE EMC-S since 2011, and session chairs of many international conferences. He also serves as the reviewer of IEEE Transactions on several topics, and other primary electromagnetics and microwave related journals.